Image Processing Assisted Algorithms for Optical Projection Tomography

Abbas Cheddad*, *Member, IEEE,* Christoffer Svensson, James Sharpe, Fredrik Georgsson, and Ulf Ahlgren*

Abstract- **Since it was first presented in 2002, Optical Projection Tomography (OPT) has emerged as a powerful tool for the study of biomedical specimen on the mm to cm scale. In this paper we present computational tools to further improve OPT image acquisition and tomographic reconstruction. More specifically these methods provide: (A) semi-automatic and precise positioning of a sample at the axis of rotation (AR) and (B) a fast and robust algorithm for determination of post alignment values throughout the specimen as compared to existing methods. These tools are easily integrated for use with current commercial OPT scanners and should also be possible to implement in "home made" or experimental setups for OPT imaging. They generally contribute to increase acquisition speed and quality of OPT data and thereby significantly simplify and improve a number of three-dimensional and quantitative OPT based assessments.**

Index Terms—**Biomedical image processing, optical projection tomography, pancreas, islets of Langerhans, artifacts, post-alignment, axis of rotation.**

I. INTRODUCTION AND BACKGROUND

Optical projection tomography (OPT) could be viewed as the optical equivalent of X-ray computed tomography (see Fig. 1 and [1]), and was initially introduced as a novel technique for three-dimensional (3D) visualization of embryonic scale specimen [2]. As such, the technique has already contributed to a large number of studies aimed at addressing a broad range of biological questions in diverse systems such as human, mice, chicken, fly, zebrafish and plants (see e.g. [3]-[8]).

* A. Cheddad, U. Ahlgren and C. Svensson are with the Umeå Centre for Molecular Medicine, Umeå University, S-901 87 Umeå, Sweden (phone: +46907854420; fax: +46907854400; e-mail: abbas.cheddad@ucmm.umu.se; ulf.ahlgren@ucmm.umu.se; christoffer.svensson@ucmm.umu.se).

F. Georgsson is with the Department of Computer Science, Umeå University, S-901 87 Umeå, Sweden (e-mail: fredrikg@cs.umu.se).

J. Sharpe is with the ICREA, EMBL-CRG Systems Biology Unit, Centre for Genomic Regulation (CRG), UPF, Barcelona, Spain (e-mail: james.sharpe@crg.eu).

More recent adaptations have further enabled the use of the technique for studies of specimen on the adult mouse organ scale [9], individual cell nuclei [10] and for longitudinal assessments of organ cultures [11]. However, as with any young technology, OPT is associated with a number of technological hurdles. In the case of OPT, these most commonly relate to artifacts introduced by the tomographic reconstruction process itself or to those of an optical nature. Improved protocols to circumvent such obstacles will directly impact on the accuracy by which OPT can be used for visualization and quantitative assessments of biomedical specimens. One example where such improvements are highly called for comes from studies of the mouse pancreas, which is the dominant model for studying the genetics and progression of diabetes disease aetiology. The pancreas is composed of small insulin-producing micro organs, the islets of Langerhans, which are scattered in thousands throughout the much greater exocrine parenchyma. The scattered organization of the islets in combination with the size and optical properties of the gland put high demands on the tools utilized. We have previously demonstrated the capacity, by OPT, to visualize and to quantify the islet insulin-cell (β-cell) distribution throughout the volume of the gland, down to the level of the individual islets [9], [12]. These assessments however were dependent on protocols involving an unwanted degree of subjectivity [9], [13], [14]. The pancreas thus appears as a good example of a structurally complex organ that is generally considered "challenging" from an imaging point of view, be it by OPT or by other imaging modalities [15]. We have therefore selected to illustrate the functionality of the developed computational tools primarily using this organ system. However, as demonstrated by OPT imaging of other specimen (including mouse liver and embryonic gut) these tools may be easily integrated into OPT based assessments of other organs or tissues, using currently available commercial, "home made" or experimental set ups for OPT scanning.

Towards the goal of generating high-quality undistorted OPT tomographic reconstructions we propose the following; 1) A pre-acquisition automatic calculation of the displacement distance needed for aligning a sample at the axis of rotation (AR), discussed in sub-section II-A, with comparison to existing methods. 2) A precise (with a precision of 0.01pixel as proven in the referenced literature) post-acquisition alignment detection and correction algorithm, exploiting the recently introduced single-step discrete Fourier transform (DFT) approach, that eliminates subjectivity in choosing the

alignment values, Δγ, (sub-section II-B). Section III presents comparison to other methods and shows some tomographic reconstruction results. Finally, concluding remarks are drawn in section IV.

II. METHODOLOGY

For maximum reconstruction quality, the sample must be optimally placed on the axis of rotation (AR). This manifests itself as a pre-scan translation of the region of interest with respect to the AR, in both directions (X Y) in the 3D world, which correspond to translations along the x-axis in the 2D image coordinate system. The specimen is fixed on a magnetic mount attached to a central shaft and therefore no correction is needed along the Z-axis, i.e., no vertical drop is associated with our scans; see Fig. 2a. In the following sub-section, we describe an approach based on image processing to aid in aligning the sample at the AR (correction of X, Y misalignments). This process could easily be made automatic and fully integrated into the scanner. Sub-section B highlights the correction for the second deviation, post-scan shifts along the x-axis in the 2D world. For the below sections, the algorithms were implemented using MATLAB ver 7.11.0.584 and IP Toolbox ver. 7.1 running on a 64-bit workstation running Windows XP and 16.GB of RAM, 2.99 GHz.

A. Selecting and positioning a region of interest (ROI) on the axis of rotation

Background and motivation

The arbitrary mounting of a specimen on the OPT scanner's motor requires an efficient way to position a specimen at the AR. Inaccurate positioning of the specimen at the AR results in unwanted blurring effects after reconstruction of sinograms. How intense this artifact is depends on the distance of the region of interest from the axis-of-rotation (AR). Moreover, AR misalignment causes the specimen to oscillate from side-to-side during a rotational image capture, limiting down the magnification needed to keep it in view [16].

In most cases specimens are not of homogenous structure and therefore it is not intuitively obvious where the ideal centre of the specimen lies. To the best of our knowledge, there is currently no objective method to allow for a pre-acquisition determination of the distance of the sample centre to the AR in OPT. This determination is also an issue for single photon emission computed tomography (SPECT) as shown in a recent study by Hyun Kim et al. [16]. They describe a laser-based alignment system, which provides a physical approach towards solving the problem in SPECT with a pinhole collimator. However, translated to OPT imaging, this setup would require additional mechanical resources to be fitted into the OPT architecture. In contrast, the work described in this manuscript is a software-based system and therefore highly integratable.
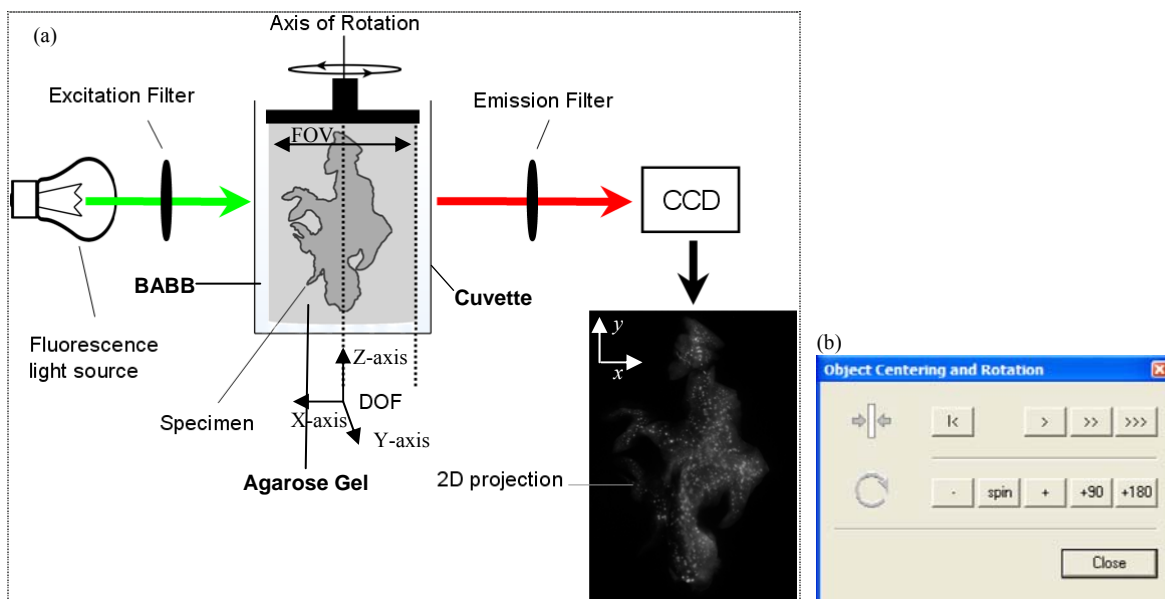

Fig.1. A simplified schematic view of the OPT set-up (emission-OPT). (a) A fluorescent antibody labeled specimen is embedded in agarose and made semitransparent in an organic solvent (typically a mixture of benzyl alcohol and benzyl benzoate). Images are recorded on a CCD chip throughout a full 360° rotation. Using computer software the original 3D information is subsequently recalculated. In emission projection tomography the specimen is exposed to an excitation light (green) and as a result the fluorochrome labeled antibody emits light (red), which is captured on a CCD chip. Of note, in emission OPT the signal from endogenous tissue fluorescence may in most cases be used to recreate the outline of the specimen. This channel, which is normally collected in the green spectrum, is referred to as the "anatomy" channel. The sketch also illustrates the axis of rotation in relation to the depth of field (DOF) and (b) the manual tool provided in the SkyScan software to position a specimen at the AR. ">>>" for big steps and ">" for small steps to the right respectively.

An automated method to position the region of interest (ROI) on the AR is that of Sharpe and Perry [17] while discussing their prototype design of a rotary stage for imaging a specimen. The selection of the ROI in their method can be performed as a subjective user choice. In their system, the user is presented with four images of the specimen, rotated to 0, 90, 180 and 270 degrees. The user then manually selects where the ROI is positioned in each image, a histogram thresholding of the specimen is then applied to distinguish the specimen from the background, see column 11 (step 3) in [17]. This approach allows flexibility for the user to concentrate the scan on an arbitrary sub-region of the specimen (for example one pancreatic lobe), which means that whole-pancreas scans may not be aligned to the most optimal position. Then a fully-automated magnification-based iterative algorithm, comprising eleven steps, is triggered, each time calculating (1) with four acquired views and correcting for the total displacements along the X and Y axes until the specimen fills up the FOV. The patent describes how to calculate the X and Y offsets, to keep the sample on the AR. The total displacements (X^t, Y^t) are then derived and applied during any subsequent rotations.[1]

$$X^t = X^d + D.\sin(\alpha+\theta), Y^t = D.\cos(\alpha+\theta)$$

where,

$$D = \tan^{-1}(X^{\alpha o}/Y^{\alpha o}), X^{\alpha o} = (X_1 - X_2)/2,$$

$$Y^{\alpha o} = (Y_1 - Y_2)/2, X^d = X^{w/2} - (X_1 + X_2 + Y_1 + Y_2)/4 \quad (1)$$

In the above equations, D represents the distance of the ROI from the stepper motor axis. X_1 is the X-position of the ROI at $\alpha=0°$, X_2 is the X-position of the ROI at $\alpha=180°$, Y_1 is the Y-position of the ROI at $\alpha=90°$, Y_2 is the Y-position of the ROI at $\alpha=270°$, and X^w is the width of the imaging window (FOV) with the term $X^{w/2}$ denoting the AR.

From our perspective the hardware stage presented in the patent would, if implemented, appear useful from a practical point of view.

In the following section, we describe our proposed method (COM-AR) that requires only two projections, 0 and 90 degrees, corresponding to the X and Y directions, which are sufficient to define a motion path around the AR. We use a computerized calculation to find the region of interest (using the GFP-anatomy channel), which is in our case the center of mass (COM), rather than allowing arbitrary ROIs. The algorithm is tested on real heterogeneous shaped specimens. The obtained results show that two views are all what is needed to determine the required displacements to an accuracy of less than ¼ pixel.

---

[1] In this section, and from this point onwards, we shall use (x y) to refer to a point in the 2D image coordinates, and (X Y Z) in the 3D world coordinates.

Proposed method (COM-AR)

To make the problem tractable at the pre-acquisition level, i.e., before the scan starts, two views of the specimen are previewed and exported, namely rough estimates of the projection with the largest possible area of the imaged specimen (view$_1$), treated as $0°$ view associated with the X-axis, and its $90°$ view (view$_2$), associated with the Y-axis, for both the anatomy and signal channels. These views define the planes of motion. Unlike the pancreas, which is heterogeneous in shape, these views are normally easy to identify in more symmetrical objects. The rationale behind using the anatomy channel, a quasi-solid object, is that its binary image often shows a better approximation of the object's shape (outline) that is not contaminated with inner details. The use of the "signal" channel, on the other hand, is to have its features form references for manual centering. Having that in mind, the algorithm goes as follows:

Suppose we have the different exported images s_a, s_s, f_a, f_s, corresponding to view$_1$-anatomy, view$_1$-signal, view$_2$-anatomy and view$_2$-signal, respectively. The ROI positioning at the AR can be seen as finding the vertical line passing through the geometric center of mass (COM) coordinates along the two orthogonal directions. To translate this representation to the real 3D world, the mounted specimen, it is sufficient to calculate the COM twice, once for view$_1$ and another for view$_2$ planes.

But before attempting that, anatomy channels need to be thresholded. It has been often the case that specimen outline is approximated using conventional thresholding [17], or by means of applying certain edge operators [18]. The two methods are useful only when there is enough contrast between image background and a signal (specimen), e.g., two distinct Gaussian distributions. However, it is not always possible to find such analytical expressions; therefore, resorting to more elaborate techniques such as the expectation-maximization (EM) method may therefore be necessary. In the EM algorithm, the maximization phase computes parameters maximizing the expected log-likelihood function derived from the 'E' step [19]. Since the EM is an iterative function, one way to speed up the convergence is to subsample the projection image without amplifying noise and here the *Haar* 2D discrete wavelet transform (DWT) comes in handy.

Suppose that we want to segment a signal from an input projection image denoted by the function f_a having the dimensions of mxn then we have

$$f_{ta} = \left| (EM[f_a^{\downarrow 2}])^{\uparrow 2} \right|, \quad (2)$$

where f_{ta} denotes the segmented signal and $|.|$ is the absolute value. Note that EM is applied only on the approximation coefficients while the other three details subbands, (i.e., $\psi_{m,n}^H, \psi_{m,n}^V, \psi_{m,n}^D$ in the horizontal, vertical and diagonal directions respectively), are zeroed out to prevent interference of high frequency signals since the aim is to obtain a binary

image. It is possible to apply the EM on lower levels; however, it is sufficiently accurate for most practical purposes to restrict that to two levels only which are shown in (2) by the inner arrow for down-sampling and the outer arrow for up-sampling.

Now, if the thresholded binary images of s_a and f_a using (2) are given by s_{ta} and f_{ta} respectively, then COM points (x coordinates) are derived by

$$\bar{x}^{s_a} = (\sum_{x,y \in \ell_s} s_{ta}(x,y))^{-1} (\sum_{x,y \in \ell_s} s_{ta}(x,y)x)$$

Similarly, $\bar{x}^{f_a} = (\sum_{x,y \in \ell_f} f_{ta}(x,y))^{-1} (\sum_{x,y \in \ell_f} f_{ta}(x,y)x)$ \hfill (3)

where ℓ_i signifies the specimen area in the two projections which is easily obtained by voting for the largest labeled connected component in the 2-D binary image, and $\bar{x}^{s_a}$, $\bar{x}^{f_a}$ are the COM x-indices of view$_1$-anatomy and view$_2$-anatomy, respectively.

Hence, the corresponding translation offset shown in Fig. 2 (a, bottom), where lines passing through COM and AR must totally overlap, is in fact analogous to a spatial shift along the X axis (view$_1$) and Y axis (view$_2$) as indicated by the top tiny arrows in Fig. 2 (b). This fact reinforces the requirement for only two projections as discussed earlier. In Fig.2 (b) the parallel vertical lines correspond to AR and the line passing through the COM point in each view. The tiny arrows on the top show the X and Y distances of the center of the specimen from the axis of rotation (AR) of the primary stepper motor. This distance could very easily be measured in pixels and converted to stepper motor units (displacements of the 3D position in μm) as the zoom factor is a known parameter. However, we stop at this stage and supply the user with view$_1$ and view$_2$ with the specimen COM lines superimposed on the two images acting as reference points allowing manual-referenced centering of the specimen at the AR so that the sample could spin on its own axis.
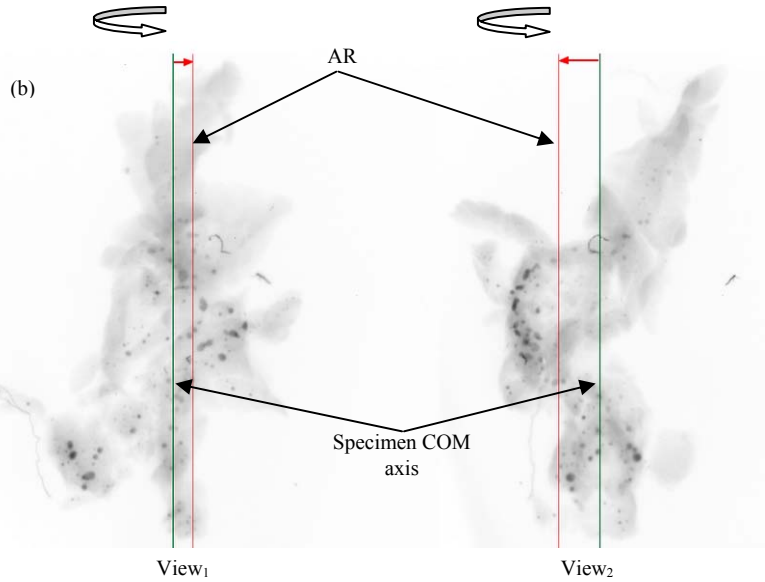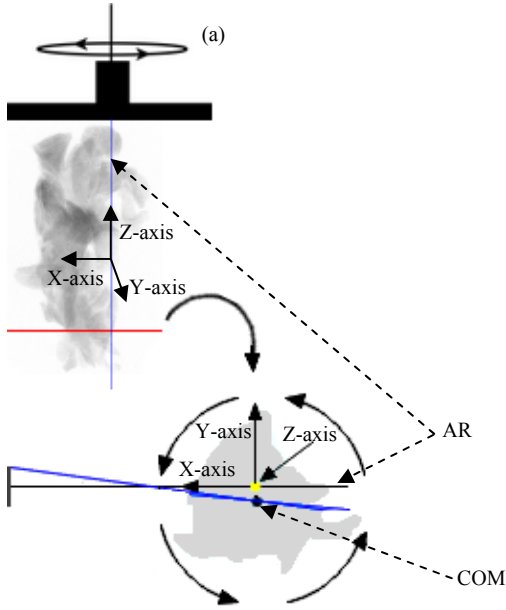

Fig. 2. Specimen positioning at the correct AR. (a) Graphical model of a tomographic slice from the GFP-anatomy channel (8 weeks female C57BL/6 mouse dorsal pancreas) depicting the relationship between the axes associated with 3D imaging. Note that the positioning solution is the one which results in translations along the X and Y axes so that the AR passes through the COM. (b) 0° (view 1) and 90° (view 2) projections (emission OPT) of a mouse pancreas labeled for insulin (dark areas). The above alignment scenario can be achieved via a global synchronization of the two shown axes in both views. Images are inverted and gamma enhanced to increase clarity.

Taken together, the AR and COM mismatch is therefore resolved by means of digital image processing. The algorithm provides a stable performance even when having a severe blurriness (out of focus) as depicted in Fig.A3 in the Appendix. Note that the described COM based alignment applies primarily to samples where the entire specimen forms the ROI. To contrast the effectiveness of the algorithm, we generate an off-axis scan of a pancreas and a control scan using the described COM automatic alignment at the AR. In order to eradicate any bias, the reconstruction is carried out using the filtered back-projection (FBP) algorithm, post-alignment is roughly tuned for both scans and the intensity dynamic range is uniformly set across all sections and for both scans allowing some background tissue noise and ring artifacts to appear. The purpose hereby is to form an unbiased analysis of the effect of COM mis-positioning. Cross-section top views of the two scans are shown in Fig. 3 (a, b) and the effects on spatial intensity is depicted in Fig. 4. To conclude, the AR-COM mismatch is characterized by a blurring effect and not by the ghost-shadow layer shown in Fig. 5.
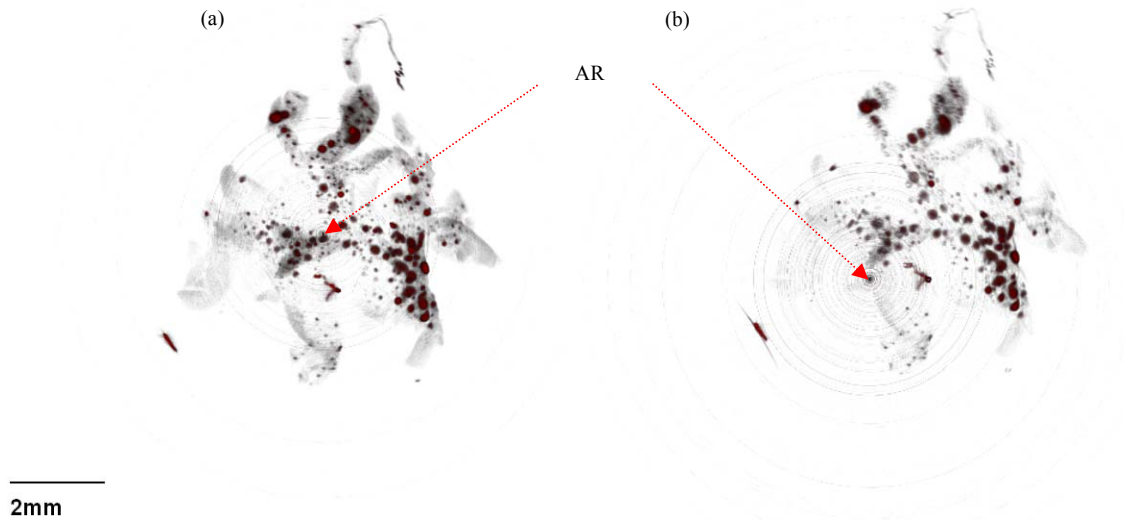
2mm

Fig. 3. A visual comparison of the effect of on versus off-axes positioning on tomographic section data. (a) A tomographic cross-section of a mouse pancreas shown in fig. 2b scanned using, the COM-AR method for aligning the sample at the AR, the ring artifacts are deliberately left since they are all perfectly centered at the true AR allowing validation of the precision of the COM-AR algorithm. (b) Off-axis positioning at the same level as shown in (a).
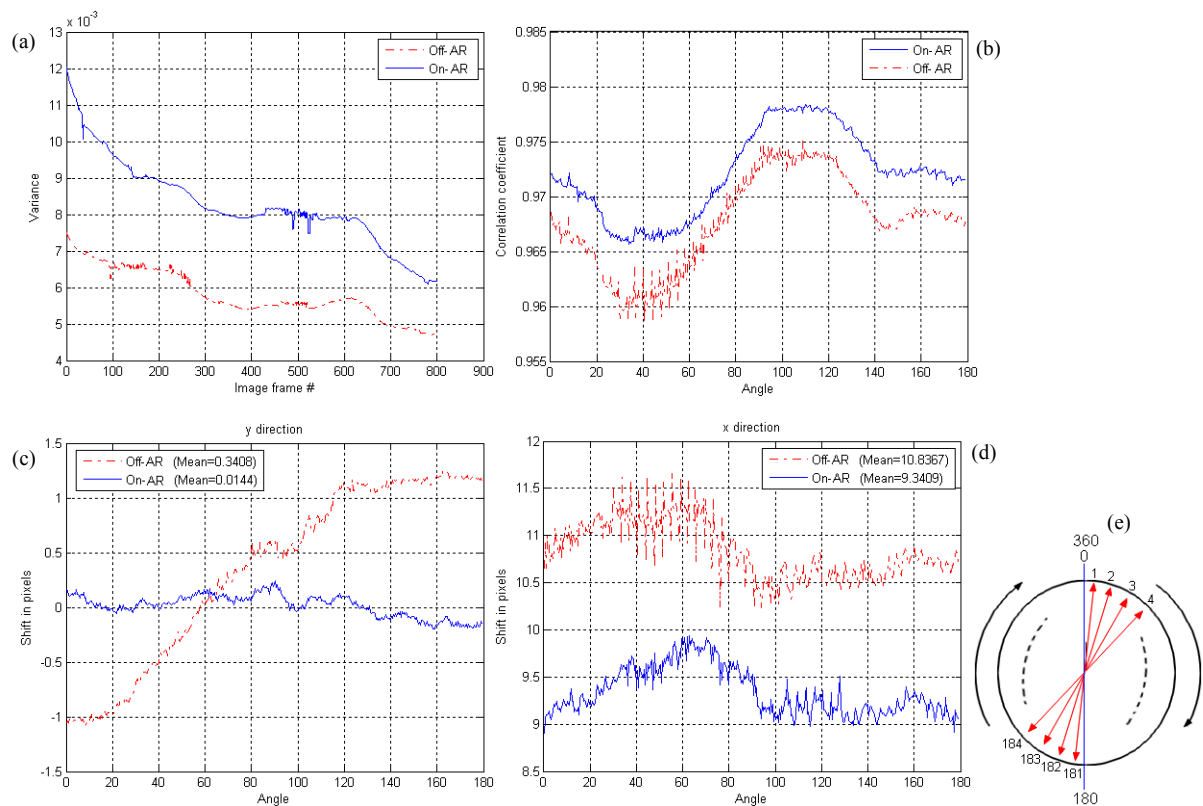

Fig. 4. A pronounced spatial improvement gain is obtained when using the COM-AR. (a) The focus is enhanced throughout the sample, when applying the proposed COM-AR algorithm. (b) Diagram depicts the improvement of correlation between parallel projections (as sketched in Fig. 4 *(e)*) of the scanned raw data using the described method and off-axis quantified by correlation coefficients. Note that the correlation between the overlapping first and last frames (0° and 360°) ideally equals to 1, and in this experiment was 0.9904 for the proposed and 0.9810 for the off-axis scans. (c-d) The shifts measured in pixels in both *y* (c) and *x* (d) directions in the 2D projection. The shift along the *x* direction will be compensated for in the next section when we discuss the post-acquisition alignment. (e) Opposing or mirrored projections of the specimen used for comparisons in b-d.

The blurring effect is caused by acquiring out-of-focus projections as can be seen in Fig. 3 (b). In Fig. 3 (a), the specimen is well centered at the AR assuring the best focus of most of the detail. This agrees reasonably with a second characteristic, a well aligned sample at the AR helps improve the correlation between $\{0°,(180°)^T\}$ and $\{90°,(270°)^T\}$ projections after mirroring the latter projections with the transform T, see Fig. 4. The former angles are used in Section B. As can be expected, the correlation is never around perfection, 1, owing to physical constrains (e.g., fiber and other particles floating around the specimen in BABB, a clearing agent, or captured within the agarose), photo bleaching, tissue thickness, light scattering or to minor shifts along the x-axis in the 2D projections (this factor is compensated for by using post-alignment corrections which is discussed in the next sub-section). This phenomenon is also observed in SPECT/CT. An exact alignment can be lost either by poor calibration of the relative position of the modalities' isocenters or by a change in the SPECT centre of rotation [20].

B. Post-acquisition misalignment detection and correction

Background and motivation

The 2D horizontal misalignment can be approximated by comparing scanned images corresponding to the two projections at $\theta \in \{0°,(180°)^T\}$, where T denotes the mirror spatial transformation, i.e., horizontal flip. In an ideal world, the two should perfectly correlate, hence $\Delta\gamma=0$. The latest version of the well-known reconstruction package, Nrecon[2], employs a least-square minimization algorithm to achieve the post-alignment [21].

A post-correction attempt is made by Walls et al. [22] where it is demonstrated that a reconstruction with an incorrectly identified AR can be regarded as a convolution of the correct signal and a blurring function. The maximum variance is then calculated from a series of variances corresponding to reconstructions of the same slice having different AR positions. In their view, this maximum value pinpoints the ideal reconstruction as it is assumed to be the least blurred. We argue that this dependency on the variance is a less safe measure since the variance is a statistical descriptor of intensity distribution that can be deceived by the chosen dynamic range used in reconstruction. This technique is borrowed from the "autofocus" correction field in 2D images [23]. The case with 3D stacks may demand further verification of generalizing the found AR position to the remaining tomographic slices. This is because the said blurring function is more likely to be non-constant along the Z stack. Nevertheless, Birk et al. [24] adopted Walls et al.'s technique

where they refer to the AR deviations as longitudinal shifts; Meyer [25] followed the same method. It is noted in Walls et al. [26] that reconstructed OPT images experience blurring effects that worsens with increasing distance from the AR. However, the *ghost shadow* effect shown in [26], namely fig. 6c therein in the reference, is more an attribute to imprecision in calculating the $\Delta\gamma$.

We observed that $\Delta\gamma$ values across the specimen exhibit a very unique pattern; see Fig. 6 (b). In the specimens utilized in this study these values gradually change in a quasi-linear fashion. This pattern re-enforces the notion that this distortion is due to the angle of the camera around the optical axis. To this end, an automatic fast algorithm to compensate for the miss-alignment, benefiting from the recently introduced efficient sub-pixel image registration, is discussed.

Proposed method : Discrete Fourier Transform Alignment (DFTA)

Image registration is extensively studied in the literature and various methods have been proposed. In this work, images are registered in the Fourier domain following the single-step DFT (SDFT) approach which implements a matrix multiplication implementation of the 2D DFT to refine the initial peak location estimate [27]. The authors of this reference show that the computational time complexity of their algorithm is O(MNk), where k is an up-sampling factor, compared to the conventional inverse FFT (Fast Fourier Transform), which is $O\{MNk[\log(kM) + k(\log(kN))]\}, \forall N \le M$, where O is the asymptotic notation and MN denotes the image 2D dimensions. This is proven to be useful especially when registering large volumes of data, which is the case for OPT that produces in the range of 1000 tomographic sections with a typical resolution of 1024x1024 .

Let a reference image be denoted by, $f(x,y)$, and its spatially translated version by $g(x,y)$ shifted by $\Delta x, \Delta y$. The two-dimensional DFT of both signals are given by uppercase letters, i.e., $F(x,y), G(x,y)$, respectively. M and N are the image dimensions and (*) is the complex conjugate. The cross-correlation is thus given by the relation

$$reg_{fg}(\Delta x, \Delta y) = \sum_{x,y} f(x,y)g^*(x-\Delta x, y-\Delta y), \qquad (4)$$

which in the 2D Fourier domain is given by;

$$= \sum_{u,v} F(u,v)G^*(u,v)\exp\left[i2\pi((u\Delta x)M^{-1} + (v\Delta y)N^{-1})\right]$$

where reg_{fg} is the registered image of $g(x,y)$ based on the reference image $f(x,y)$, i is an imaginary unit used to allow for complex number calculation, x=0, 1, 2, …, M-1 and y=0, 1, 2, …, N-1 being discrete variables in the spatial coordinate system and u=0, 1, 2, …, M-1 and v=0, 1, 2, …, N-1 denoting the variables in the frequency domain.

Thus, the shift $\Delta\gamma$ is derived from the calculated peak coordinates and given by $\Delta\gamma = \Delta x/2$, dividing the error equally between the two projections, where x is the net row shift. Fig.

5 gives an example of the influence of Δγ on the reconstruction. If this value is repeatedly calculated for each section the outcome would approximate a linearly decreasing function. However, due to physical changes, which hinder arriving at a stable perfect correlation of the two projections belonging to $\theta \in \left\{0^{\circ}, (180^{\circ})^{T}\right\}$, the absolute majority of these values will adhere to this linearity. This can be regarded as an over-determined system which can be solved by a simple standard linear least squares (LLS) function, see Fig. 6, thus finding Δγ for each individual reconstructed section. The observed Δγ values behave as predicted even in the presence of some amount of noise in the projection data. Without loss of generality, the LLS(Δγ) algorithm can be described as a strictly decreasing monotonic function.

Consequently we can argue that it is sufficient to find the shift in two blocks, one at the top level of the specimen and the second at the bottom, and then interpolate the in-between sections by LLS since linearity is now assumed. As illustrated in Fig. 6a, the block size is arbitrarily chosen and is in our case eight pixels in height, which includes enough features to facilitate the correlation process.
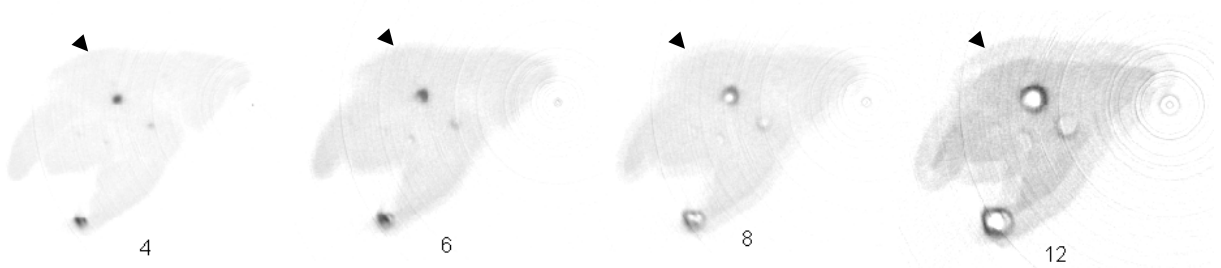

Fig. 5. Tomographic sections illustrating the sensitivity in selecting Δγ. Δγ =4 (optimum), Δγ =6 through 12 where the ghost-shadow effect gradually starts to show-up - Images are gamma enhanced to increase clarity. This recognized effect is attributed to mismatches between projections and their mirrored ones. The tomographic sections are derived from the mouse pancreas shown in fig. 2 labeled for insulin in which the islets of langerhans ideally would appear as compact oval or circular objects.

After calculating the amount of *x*-shift across the chosen sections, this range of values could be fed into the reconstruction software to perform the cone beam filtered back-projection (CB-FBP) algorithm with different values for different sections. However, if we allow for different Δγ on different sections, as is the case in [24], [25] and [22], geometric distortions will be introduced to the final reconstruction stack. Therefore, we need to determine an angle with which we rotate all the projections around a given located center to yield a unified Δγ across all sections.

Let the obtained LLS estimated function be given as $\rho_i, i = \{1,2,3...,n\}$ where *n* denotes the height of the specimen, then the corresponding angle that this straight line makes, e.g., the difference in the *y* direction in the plots shown in Fig. 8, can be computed by means of the gradient using the central difference approach which is generally a more accurate approximation to the first derivative than the forward difference.

$$\nabla m_y = \frac{\partial \rho_i}{\partial y}, \therefore \theta = (\nabla m_y /(\pi /180)) \qquad (5)$$

The calculated angle, θ, is in degrees. In order to rotate the projections in the correct manner, the rotational centre point must be located. The *x*-coordinate of this point is the index point where the corresponding post-acquisition alignment magnitude is zero or approaches it, i.e., $|LLS(\Delta\gamma)| = \sqrt{(LLS(\Delta\gamma))^2} \approx 0$. By using the COM-AR discussed in (section *A*) the *y*-coordinate would be *M/2* where *M* is the number of columns in the projection image. Depending on how far the *x*-coordinate is from the center of the image, all projection images, i.e., 0°-360°, must be padded with a blank array as illustrated in Fig. A2, in the Appendix, and the algorithm therein.
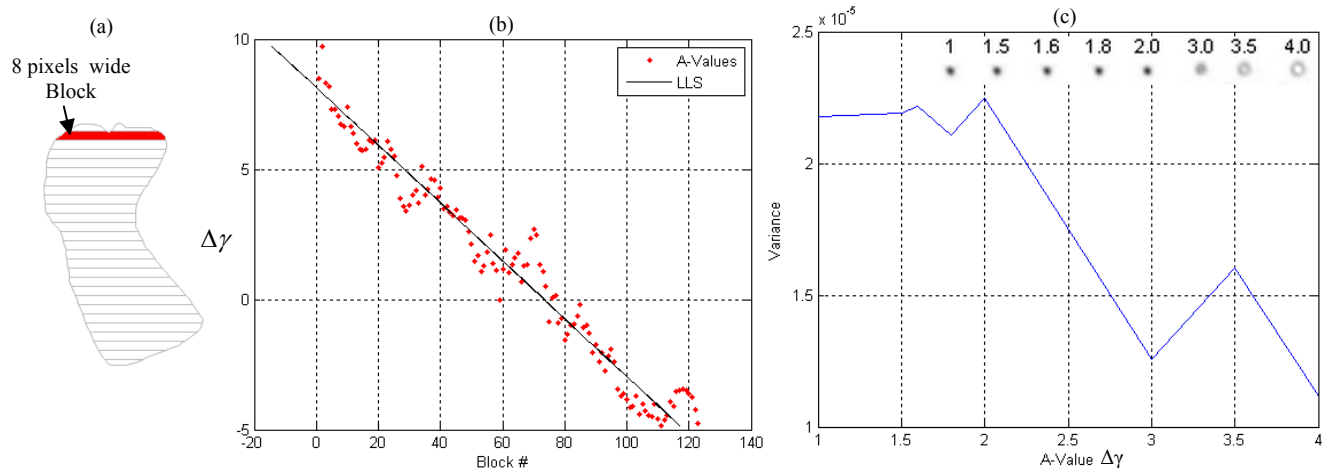
Fig. 6. The DFTA method facilitates Δγ tuning without the need for multiple reconstructions. (a) The specimen is virtually divided into 128 blocks, each block being 8 (1024/128) sections wide. Theoretically speaking, it is possible to obtain Δγ for each individual section. (b) An experiment on a mouse pancreas, Δγ is depicted as scattered points for each block and the fitted LLS function is shown as a solid line. (c) Calculated variance of a section reconstructed under different Δγ. Shown on the top right corner is the same islet cropped from the different reconstructions, the highest variance was found at Δγ =2.0 while the presented algorithm voted for Δγ =1.8, which has almost an identical reconstruction. Our proposed automatic DFTA directly pinpoints the best value, thus eliminating the need for multiple reconstructions used in the variance-based voting method [24], [25], [22].

After obtaining the corrected projections (*Corrected_Proj*), the Δγ can be recalculated, which should ideally be a constant zero, but due to numerical variations the mean of the values can be used instead to reconstruct the entire volume as shown in Fig. 7. The seamlessly rotated projections do not show any inconsistencies in the final reconstruction, e.g., ridges, geometric artifacts or discontinuities. In fact, the LLS-Gradient based rotation not only provides a unified Δγ solution for the entire volume but eventually it also increases the reconstruction quality as proven by the achieved high correlation between opposing projections and the reduced (*x, y*) shifts, see Fig. 8 and the volume rendering depicted in Fig.14.
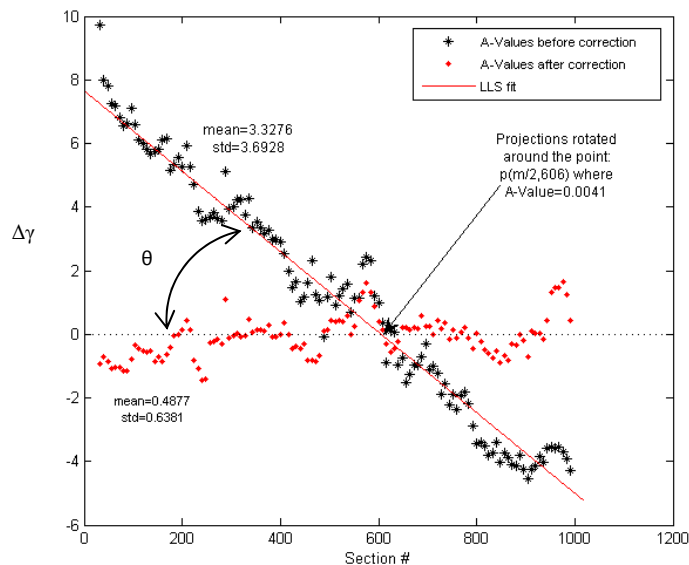

Fig. 7. Comparison of the A-Values (Δγ) obtained across sections of different specimens before and after applying the LLS-Gradient based correction. The rotation is carried out around a new central point *P(M/2, Index)* ultimately bringing the mean of the Δγ close to zero. The angle made by the line is obtuse, hence its gradient is negative, i.e., rotating the projections clockwise in our MATLAB implementation, with $\theta = -0.7389$ in this example.
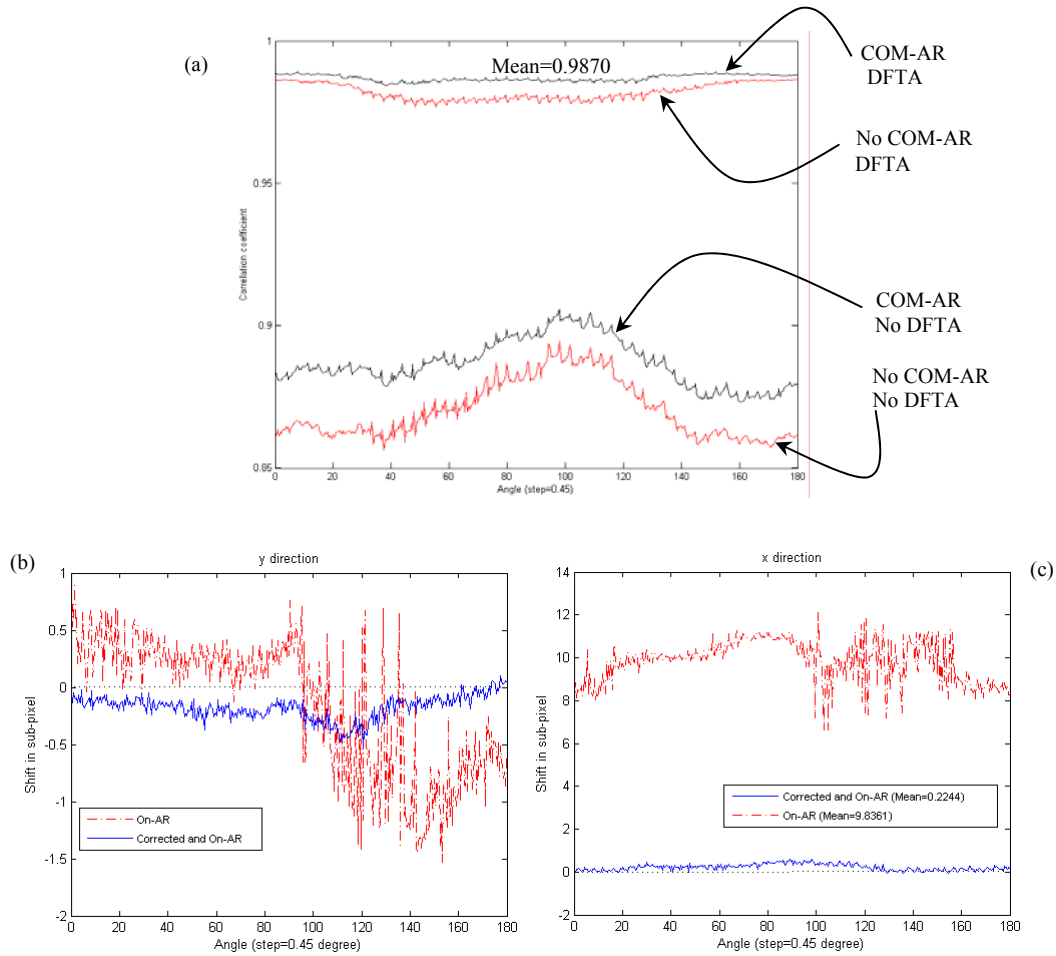
Fig. 8. Diagrams illustrating the combined effects of the proposed COM-AR and DFTA correction. (a) The plot shows the cross correlation coefficient of projections and their horizontally flipped mirrored images. It is evident that the two proposed methods complement each other in the sense that by realization of sections (A and B) we achieve a higher coefficient, which is close to perfection. (b) Calculated shifts along *y direction* in the 2D world between projections and their mirrored projections. (c) Calculated shifts along *x direction* in the 2D world between projections and their mirrored projections, contrast this result with the plot in Fig.4d.

III. RESULTS AND DISCUSSION

A. COM- AR Positioning

As previously shown in Fig. 4, having the sample well positioned at the AR helps preserve a good correlation of the opposing projections and improves the contrast (variance). This is illustrated in Fig. A1 which depicts sinograms and tomographic reconstructions derived from on- and off-axis of rotation scans. As shown in Fig. A3, finding the COM is not drastically affected by acquiring out-of-focus images. The test displayed in this figure was designed to assess the accuracy of the COM calculation method and therefore it should be noted that the presented images are synthetically blurred (post-processing) since OPT scanners typically have a large DOF (in our case 15mm at the lowest magnification and 1.5mm at the highest magnification). The experiments, herein, indicate that the COM-based method is less sensitive to blurriness because of the following:

- The COM works on binary blobs and is not the intensity weighted COM.
- These binary blobs are obtained using a combination of two powerful techniques:
  o 2D DWT: The image is initially decomposed into high and low frequencies using 2D discrete wavelet transformation (2nd level), and
  o EM: The expectation maximization algorithm is then invoked to robustly segment out a given specimen (binary blob). Note that GFP channel is used for this purpose. EM is a well-recognized method in the object segmentation field, which is robust against various types of image processing filtration.

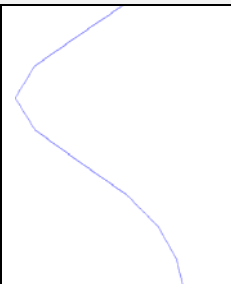### B. Comparison of DFTA correction against existing methods

As illustrated in Fig. 9, relying on variance-based correction may provide a less attractive solution for

determining the $\Delta\gamma$. Compared to [24], [25] and [22], the method described herein yields a faster solution with a higher precision. In contrast to the previous mentioned studies, where multiple reconstruction iterations are induced for tuning based on a vote for the highest score of the variance, the process of finding each value in the vector $\Delta\gamma$ is carried out only once using the DFTA; see Table I and Fig. 9. In the following section (the results presented in table I, II and Fig. 9-11), the experiments was designed in such a way that the calculation of variance conformed to Walls et al.'s description quoted below.

> *"The position of the rotational axis can then be determined by reconstructing a series of images with differently assumed positions of the rotational axis, and calculating the variance of each reconstruction. The reconstructed image that has the maximum variance is closest to the ideal reconstruction, as it is the least blurred."* [22].

TABLE I
PERFORMANCE COMPARISION OF VARIANCE-BASED CORRECTIONS AND THE DFTA

[24], [25] and [22]			DFTA	
Variance				
Rec (1)	3178.2271		*Rec (DFTA) = 7941.0959*	
Rec (2)	5115.2187			
Rec (3)	6994.5275			
Rec (4)	*7792.6737*			
Rec (5)	6990.7245			
Rec (6)	5100.7684			
Rec (7)	3227.8390			
Rec (8)	1902.2256			
Rec (9)	1165.6381			
Rec (10)	831.31030			
Other criteria				
Elapsed Time		3.4966 min	1.3925 min	
Number of Trials		10	1	
Step		0.5	N/A	
Selected Reconstruction		Rec (4)	Rec (DFTA), Fig. 9	
Selected $\Delta\gamma$		7.5	-0.5	
Number of possible sections to be reconstructed with this value ($\Delta\gamma$)		1	1024 (entire stack)	

Optimization using variance instead of SDFT: In the phase of image registration, Section II (B), we consider finding misalignments by means of SDFT, a technique proposed by Guizar-Sicairos et al. (2008). Fig. 10 and 11 compare the performance of SDFT against the statistical variance method. In Fig. 10, the superimposed circles highlight blocks where the variance is a poor descriptor. This imprecision to some extent misleads the calculation of the LLS-gradient, which in turn affects computing the rotation angle. Table II tabulates this effect.

Rec(1) Δγ = 9.0   Rec(2) Δγ = 8.5   Rec(3) Δγ = 8.0   *Rec(4) Δγ = 7.5*

Rec(5) Δγ = 7.0   Rec(6) Δγ = 6.5   Rec(7) Δγ = 6.0   Rec(8) Δγ = 5.5

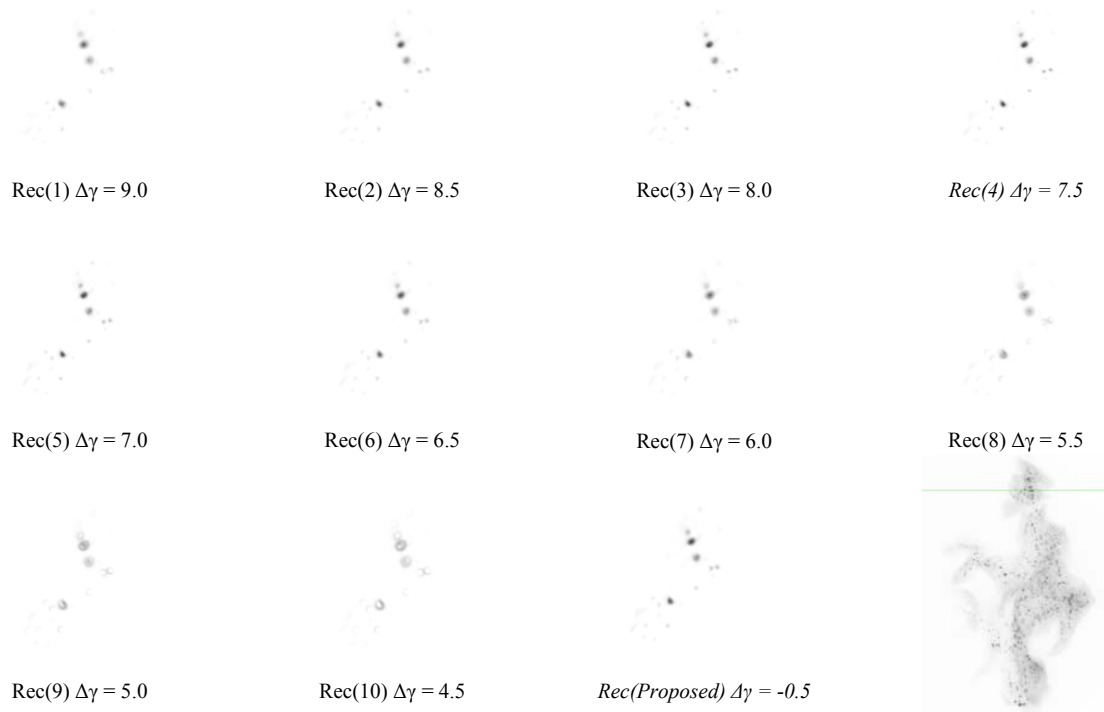Rec(9) Δγ = 5.0   Rec(10) Δγ = 4.5   *Rec(Proposed) Δγ = -0.5*

Fig. 9. Visual comparison of variance-based corrections and DFTA corresponding to the data presented in table I. The figure shows reconstructions of a single section corresponding to the green line in the projection image (lower right, 8 weeks female C57BL/6 mouse dorsal pancreas) Rec(1-10) are reconstructions based on different Δγ values used as input to vote for the highest variance which eventually has promoted Rec(4). Contrast this with the reconstruction using the DFTA Rec(Proposed). Similar data for other specimen types are presented in Fig. S1 and Fig. S3. Note that the elapsed time of the variance-based method was 3.4966 min, which corresponds to more than half an hour if a given sample is divided into 10 blocks. For DFTA the elapsed time was 1.3925 min in which 1024 sections were corrected.
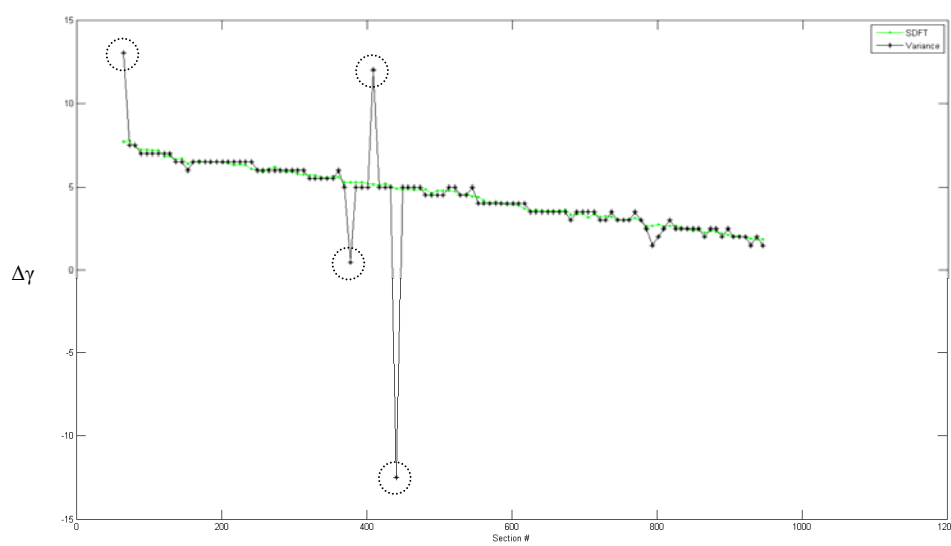

Fig. 10. Comparison of calculated Δγ using the statistical variance versus the SDFT algorithm. The superimposed circles highlight blocks where the variance is a poor descriptor. Similar results were obtained using other specimens (see supplementary Fig. S5).
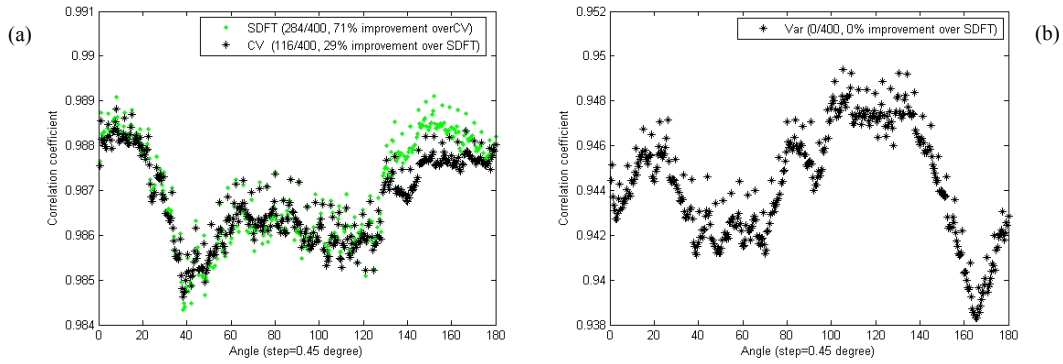
Fig. 11. Comparison of cross correlation coefficients of the projections and their horizontally flipped mirrored images of the variance-based correction versus SDFT. (a) SDFT (green dots) versus CV (the refined variance after supervised suppression of poor values, shown as black stars). (b) Coefficients' plot of the corrected projections using the unaltered variance in Fig. 10.

TABLE II
PERFORMANCE COMPARISION WHEN USING VARIANCE IN CALCULATING THE X-SHIFT (SECTION IIB) AGAINST SDFT

Method/Criterion	Elapsed Time (A block is 8 pixels wide)	Angle	Index (x_o)**	Mean Correlation (Fig. 11)	Accuracy
Variance	17.7543 sec (128 partitions)	-0.8298	817	0.9444	94.4353%
Refined Variance* (CV)	17.7543 sec (128 partitions)	-0.3835	1215	0.9868	98.6770%
Single-step DFT (SDFT)	4.8225 sec (128 partitions)	-0.3456	1278	0.9870	98.6958%

(*) The refined variance is the variance vector with poor estimators, shown within circles in Fig. 10, being eliminated from the calculation of the line equation and thereafter the angle. (**) see the Algorithm pseudo-code in the Appendix.

C. Tomographic Reconstruction Results

A phantom was prepared using a glass capillary with known inner diameter (the diameter of the tube was measured beforehand using high-resolution microscopy). The objective of this phantom, of known properties, was to measure the amount of shape deformation of the reconstructed data as compared to the ground truth. Two reconstructions were generated from a single OPT scan, one implementing the DFTA and another using the variance-based, see Fig. 12.
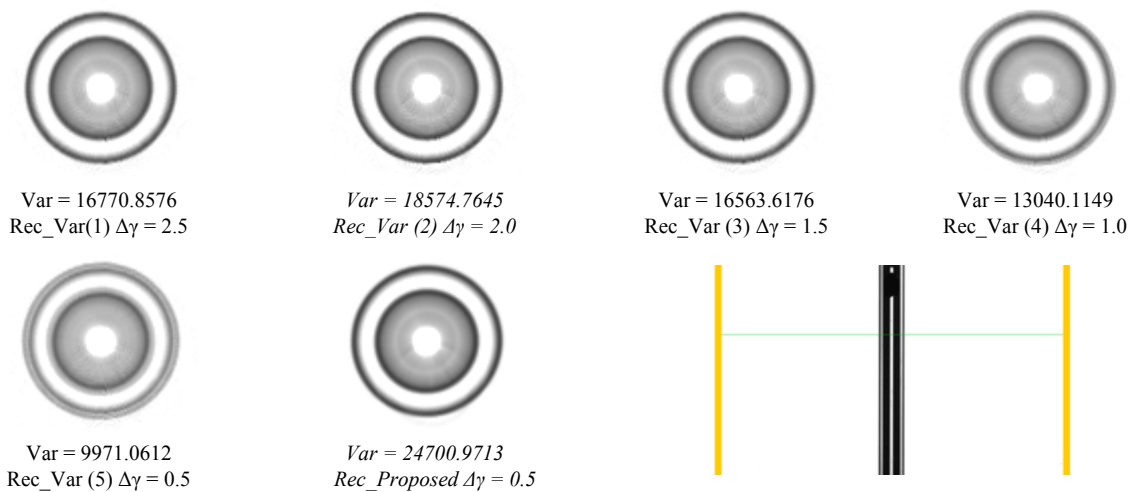

Var = 16770.8576
Rec_Var(1) Δγ = 2.5

Var = 18574.7645
Rec_Var (2) Δγ = 2.0

Var = 16563.6176
Rec_Var (3) Δγ = 1.5

Var = 13040.1149
Rec_Var (4) Δγ = 1.0

Var = 9971.0612
Rec_Var (5) Δγ = 0.5

Var = 24700.9713
Rec_Proposed Δγ = 0.5

Fig. 12. Visual comparison of variance-based corrections and DFTA carried out on a glass capillary phantom (inner diameter 700μm ±10μm). Rec_Var (1-5) shows the different reconstructions required to vote for the best reconstruction. The chosen reconstruction was the one with highest variance score, Rec_Var(2). Lower right shows a projection view of the glass tube before reconstruction. The green line indicates the level at which the shown sections were generated. Note that Rec_Proposed shown above was obtained using a single reconstruction only.

Fig. 13a reaffirms the notion that the uncorrected Δγ can be described as a strictly decreasing monotonic function. In order to quantify the improvements that this work brings about, we recalculated the diameter after scanning and reconstruction,

i.e., after the CB-FBP and dynamic range settings were applied. As illustrated in Fig. 13a, the DFTA clearly increments the quality of the reconstructed data. Fig. 13b illustrates the calculated diameter using both the proposed and the variance-based reconstructions; it is evident that the diameter after $\Delta\gamma$ correction is more stable across all sections. The standard deviation (*std*) of the variance-based method was 19.2977 while for DFTA it was 1.9451.
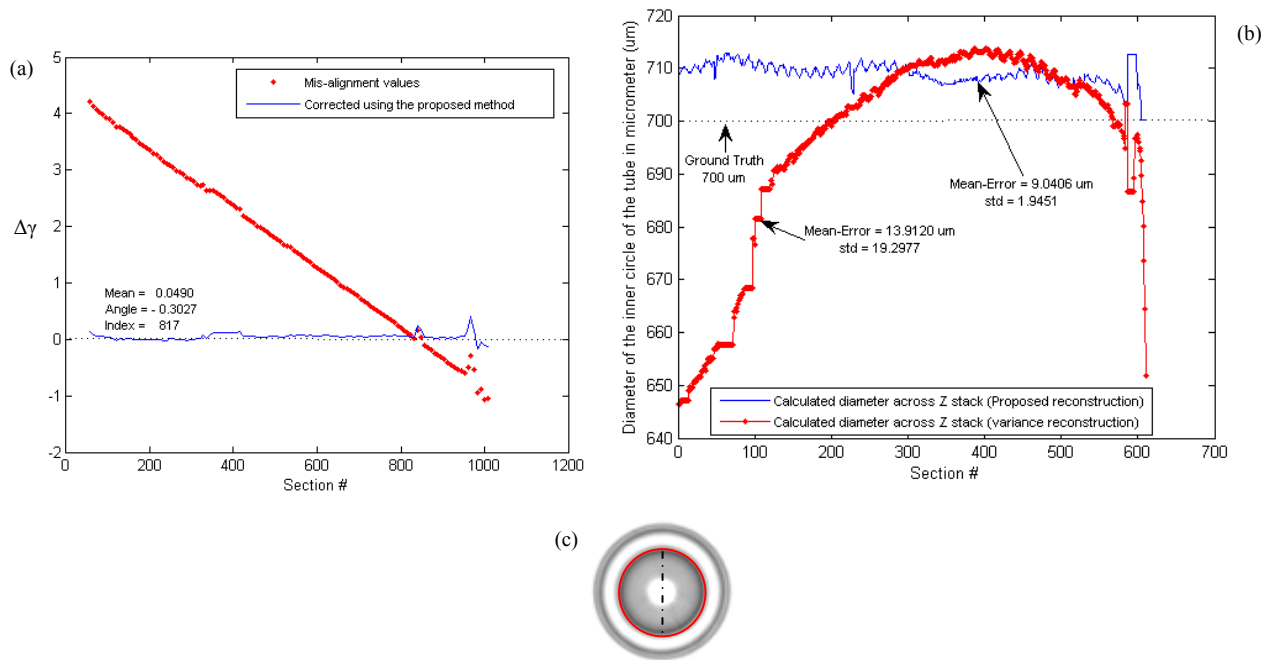

Fig. 13. Comparison of the variance-based method and the DFTA when applied to a glass capillary phantom with known diameter. (a) $\Delta\gamma$ before and after correction using the DFTA. (b) Calculation of the inner circle diameter,(broken line in (c)) using the variance-based method (red line) and DFTA (blue line). Note that the calculated diameter using DFTA display less deviation from the ground truth compared to the variance-based method. (c) Tomographic section of the glass capillary. The red circle outlines the inner circumference of the tube and the broken line corresponds to its diameter.

To qualitatively assess the performance of the developed approach in the realm of real specimens applications, mouse pancreas labeled for insulin (outlining the Islets of Langerhans), mouse liver stained for smooth muscle alpha-actin (larger blood vessels) and the mouse embryonic gastrointestinal tract stained for E-cadherin (gastrointestinal epithelium) was subjected to the variance and the developed algorithms respectively (see Fig. 14 and Figs. S2 and S4). For all analyzed specimen the unitary step of rotation was set to 0.45° and the projection images were exported with a resolution of (1024x1024) in 16-bit TIF format. Hereby, the data generated using DFTA consistently produced volumetric renderings with enhanced quality as compared to the statistical-variance processed data (compare Figs. 14a and 14b).
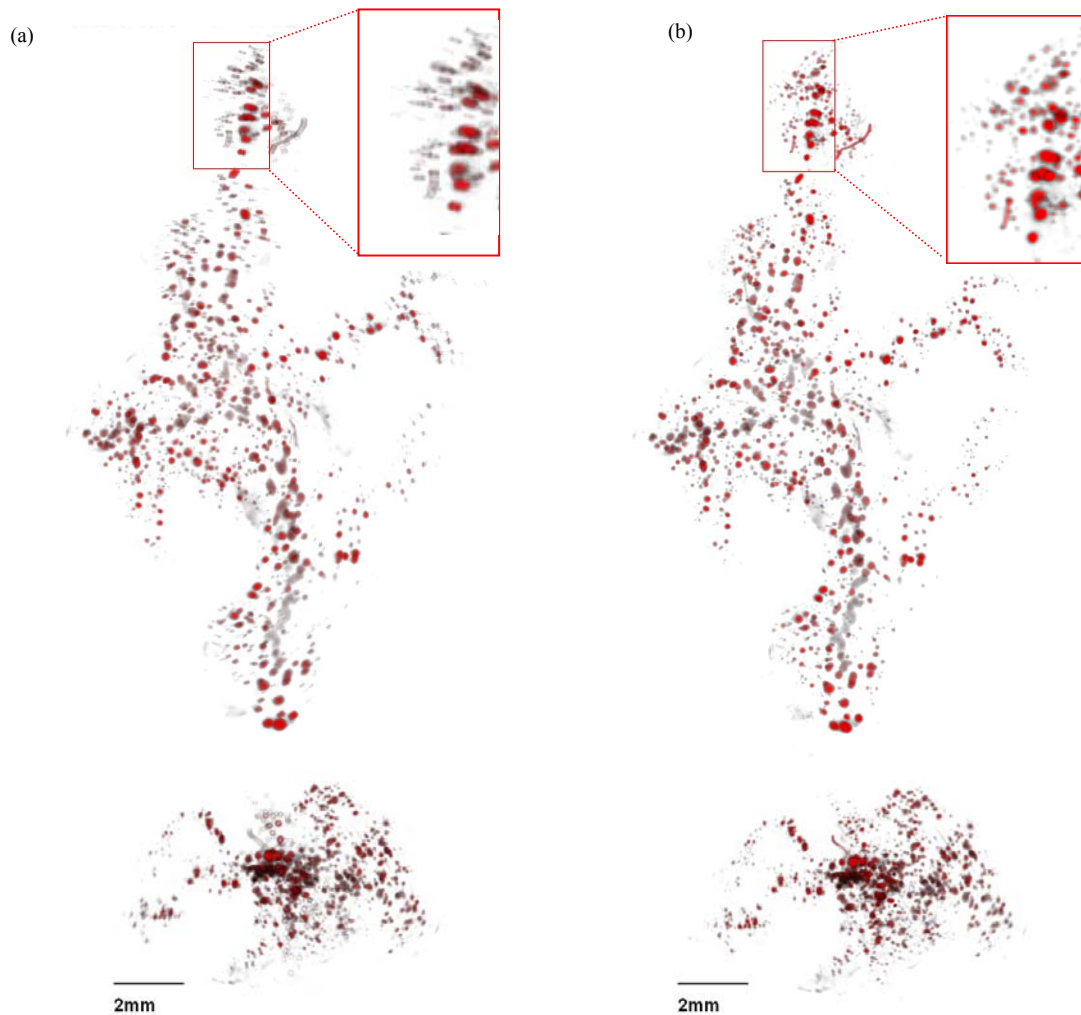
Fig.14. The proposed algorithms enhance image quality when applied to biological specimen. (a) and (b), Volume rendering of the specimen shown in Fig. 10 (pancreas labeled for insulin) using the variance-based approach (a) and the proposed approach (b). The insulin-labeled islet β-cell volumes have been pseudo-colored in red to enhance visualization and to follow the tradition in displaying specimen's in the literature. The original data, however, is monochrome. This note holds true also for the accompanying multimedia contents (supplementary videos I and II). (a) Frontal and top views of a reconstructed scan (volume-rendering) with the Δγ derived from the statistical variance based on one section, see supplementary video II. (b) The same specimen scanned and reconstructed using the proposed methods (COM-AR positioning and DFTA), see supplementary video I. Due to the degree of synchronization of two opposing projections, the dynamic range during the reconstruction was set differently between the specimens. Similar comparisons using other specimen types are shown in Fig. S2 (videos III, IV) and Fig. S4 (videos V, VI).

IV.   CONCLUSION

The term artifact, in medical imaging, characterizes every deviation of the image from the exact reproduction of the anatomical and tomographic characteristics of the area under examination [28]. Scan projections are always prone to elements, which diminish the signal-to-noise ratio as not all biological samples present significant absorption contrast [29]. The generation of high quality 3D reconstructions is a vital element in the field of molecular medicine. In this report we present algorithms that provide fast and accurate means for positioning specimen to be scanned by OPT on the correct AR and for determination and correction of post-acquisition alignment values before the reconstruction process. Obviously, the proposed DFTA algorithm inherits the shortcomings of the cross-correlation algorithm in the sense that the sample has to display sufficient features to arrive at a robust alignment. Still, as demonstrated on a variety of specimens, these algorithms contribute to reduce subjective interference in the data acquisition process and to increase acquisition speed and data quality for essentially any form of OPT based assessments conducted on biomedical specimens. The proposed approaches are further likely to impact on the possibilities to utilize OPT as a tool not only for spatial assessments but also for quantitative assessments. This comes clear when considering that typically a spatial assessment of, e.g., a proteins distribution pattern, is less dependent on small deviations in shape or object size then is a volumetric assessment of the same specimen. In the latter case, even a minor artifact induces changes, e.g., the radius of a spherical

object will cause a dramatic increase/decrease in the object's volume, an effect that will be accentuated with objects of smaller sizes. Hence, in order to perform statistically sound OPT assessments involving larger groups of specimen, e.g., when assessing deviations in islet β-cell mass in diabetes research, a fast and reliable approach to an accurate reconstruction is essential. In this respect, the algorithms demonstrated in this work can be the foundation material for a wide range of applications.

Acknowledgments

References

[1] J. Sharpe. "Optical Projection Tomography," *Annual Review of Biomedical Engineering*, vol. 6, pp. 209-228, August. 2004.

[2] J. Sharpe, U. Ahlgren, P. Perry, B. Hill, A. Ross, J. Hecksher-Sørensen, R. Baldock and D. Davidson. "Optical Projection Tomography as a Tool for 3D Microscopy and Gene Expression Studies," *Science*., vol. 296, no. 5567, pp. 541-54519, April. 2002.

[3] S. Sarma, J. Kerwin, L. Puelles, M. Scott, T. Strachan, G. Feng, J. Sharpe, D. Davidson, R. Baldock, S. Lindsay. "3D Modelling, Gene Expression Mapping and Post-mapping Image Analysis in the Developing Human Brain," *Brain Research Bulletin*., vol. 66, pp. 449-453, 2005.

[4] S. Kulandavelu Kulandavelu, D. Qu, N. Sunn, J. Mu, MY. Rennie, K.J. Whiteley, JR. Walls, N.A. Bock, J.C. Sun, A. Covelli, J.G. Sled, S.L. Adamson. "Embryonic and Neonatal Phenotyping of Genetically Engineered Mice," *ILAR J*., vol. 47, no. 2, pp.103-17, 2006.

[5] M. E. Fisher, A. K. Clelland, A. Bain, R. A. Baldock, P. Murphy, H. Downie, C. Tickle, D. R. Davidson and R. A. Buckland. "Integrating Technologies for Comparing 3D Gene Expression Domains in the Developing Chick Limb," *Dev Biol*., vol. 317, no. 1, pp. 13-23, February. 2008.

[6] L. McGurk, H. Morrison, L.P.Keegan, J. Sharpe and M.A. O'Connell. "Three-dimensional Imaging of Drosophila Melanogaster," *PLoS ONE*., vol. 2, no. 9 (e834), September. 2007.

[7]R.J. Bryson-Richardson and P.D. Currie. "Optical Projection Tomography for Spatio-temporal Analysis in the Zebrafish," *Methods Cell Biol*., vol. 76, pp. 37-50, 2004.

[8] K. Lee, J. Avondo, H. Morrison, L. Blot, M. Stark, J. Sharpe, A. Bangham, E. Coen. "Visualizing Plant Development and Gene Expression in Three Dimensions Using Optical Projection Tomography," *Plant Cell*., vol. 18, pp. 2145-2156, August. 2006.

[9] T. Alanentalo, A. Asayesh, H. Morrison, C. E. Lorén, D. Holmberg, J. Sharpe and U. Ahlgren, "Tomographic Molecular Imaging and 3D Quantification Within Adult Mouse Organs," *Nature Methods*., vol. 4, pp. 31-33, 2007.

[10] M. Fauver, E. Seibel, J.R. Rahn, M. Meyer, F. Patten, T. Neumann, A. Nelson, "Three-dimensional Imaging of Single Isolated Cell Nuclei using Optical Projection Tomography," *Opt Express*., vol. 13, no. 11, pp. 4210-23, 2005.

[11] M. J. Boot, C. H. Westerberg, J. Sanz-Ezquerro, J. Cotterell, R. Schweitzer, M. Torres and J. Sharpe, "In Vitro Whole-organ Imaging: 4D Quantification of Growing Mouse Limb Buds," *Nature Methods*., vol. 5, pp. 609-612, 2008.

[12] A. Hörnblad, A. Cheddad and U. Ahlgren, "An improved protocol for optical projection tomography imaging reveals lobular heterogeneities in pancreatic islet and ß-cell mass distribution", Islets, 3(4)(2011) 1-5.

[13] T. Alanentalo, C.E. Lorén, A. Larefalk, J. Sharpe, D. Holmberg and U. Ahlgren, "High-resolution Three-dimensional Imaging of Islet-infiltrate Interactions Based on Optical Projection Tomography Assessments of the Intact Adult Mouse Pancreas," *J Biomed Opt.,* 13(5):054070, 2008.

[14] T. Alanentalo, A. Hörnblad S. Mayans, A. Karin Nilsson, J. Sharpe, A. Larefalk, U. Ahlgren and D. Holmberg, "Quantification and Three-dimensional Imaging of the Insulitis-induced Destruction of Beta-cells in Murine Type 1 Diabetes," *Diabetes*., vol. 59, no. 7, pp.1756-64, 2010.

[15] D. Holmberg and U. Ahlgren, "Imaging the Pancreas: From Ex Vivo to Non-invasive Technology," *Diabetologia*., vol. 51, no. 12, pp.2148-54, 2008.

[16] J. H. Kim, J. S. Lee, M. J. Park, W. W. Lee, S. M. Kim, Y. K. Kim, S. E. Kim and D. S. Lee, "An Axis of Rotation Alignment System for High-resolution Pinhole SPECT Imaging," *Nuclear Instruments and Methods in Physics Research A*., vol. 589, pp. 338-344, 2008.

[17] J. Sharpe and P. E. Perry. (2007). *Rotary Stage for Imaging a Specimen*, US Patent: US 7,218,393 B2.

[18] U.J. Birk, A. Darrell, N. Konstantinides, A. Sarasa-Renedo and J. Ripoll, "Improved reconstructions and generalized filtered back projection for optical projection tomography," *Applied Optics*, vol. 50, no. 4, pp. 392-398, 2011.

[19] G. Zeng, "Iterative Reconstruction," in *Medical Image Reconstruction: A Conceptual Tutorial*, 1st Edition, Springer, 2010, p. 135.

[20] G. Gnanasegaran, G. Cook, K. Adamson and I. Fogelman, "Patterns, Variants, Artifacts, and Pitfalls in Conventional Radionuclide Bone Imaging and SPECT/CT," *Seminars in Nuclear Medicine*., vol. 39, no. 6, pp. 380-395, November. 2009.

[21] ___"Micro-Positioning v.1.0 control program and instruction manual", 27-OCT-2006 http://www.skyscan.be/products/downloads.htm, accessed on 07-Oct-10.

[22] J. R. Walls, J. G. Sled, J. Sharpe and R. M. Henkelman, "Correction of Artefacts in Optical Projection Tomography," *Phys. Med. Biol.,* vol. 50, no.19, p. 4645, 2005.

[23] F. C. A. Groen, I. T. Young and G. Ligthart, "A Comparison of Different Focus Functions for Use in Autofocus Algorithms," *Cytometry*., vol. 6, no. 2, pp. 81-91, 1985, Wiley publisher.

[24] U. J. Birk, M. Rieckher, N. Konstantinides, A. Darrell, A. Sarasa-Renedo, H. Meyer, N. Tavernarakis and J. Ripoll, "Correction for Specimen Movement and Rotation Errors for In-vivo Optical Projection Tomography," *Biomedical Optics Express*, vol. 1, no. 1, pp. 87-96, 2010.

[25] H. Meyer. (2010). *In Vivo Optical Projection Tomography in Biological Model Organisms*. Ph.D. Thesis. Erasmus Universiteit, Rotterdam, Germany.

[26] J. R. Walls, J. G. Sled, J. Sharpe and R. M. Henkelman, "Resolution Improvement in Emission Optical Projection Tomography," *Phys. Med. Biol.*, vol. 52, no.10, pp. 2775-2790, 2007.

[27] M. Guizar-Sicairos, S. T. Thurman and J. R. Fienup, "Efficient Subpixel Image Registration Algorithms," *Opt. Lett*., vol. 33, no. 2, pp. 156-158, 2008.

[28] E. Lavdas, M. Vlychou, V. Roka, G. Wozniak, G. Protogerou and I. Fezoulidis, "Artifacts in Spiral CT Protocols: The Importance of the Spatial Reconstruction," *European Journal of Radiography*., vol. 1, pp. 73-79, 2009.

[29] P. F. Feruglio, C. Vinegoni, J. Gros, A. Sbarbati and R. Weissleder, "Block Matching 3D Random Noise Filtering for Absorption Optical Projection Tomography," *Physics in Medicine and Biology*., vol. 55, pp. 5401-5415, 2010.
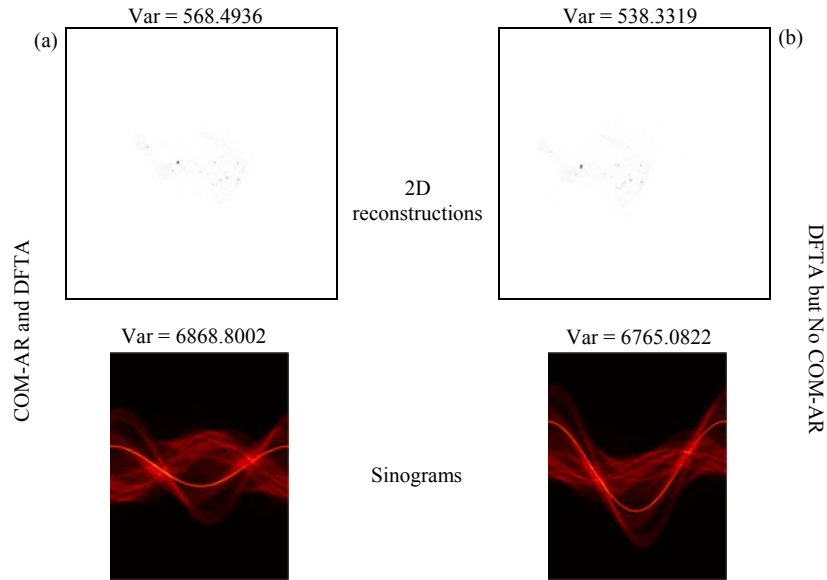
Appendix

Fig. A1. The figure shows cross section sinograms (bottom) and their respective 2D slice reconstructions (top) of a pancreas. (a) Sinogram and reconstruction of a slice from a scan using the COM-AR method discussed in Section (II A) and (b) sinogram and reconstruction of a slice on the same level using an off-center scan.

Let the *x*-coordinate index of the image new rotation center be denoted as x_o and let *MxN* be the image dimensions.

```
Padding Algorithm Pseudo-code: Rotation around the new centre (M/2, x_o)
New_Rotation_Center_Row=N-x_o;
Array_Height= |(N-(2*New_Rotation_Center_Row))|;
Offset_Blank= size (M, Array_Height);
if (New_Rotation_Center_Row >(N/2))
    Padded_image= Pad_top(Offset_Blank,Original_image);
    Proj= rotate_crop(Padded_image, θ);
    Corrected_Proj= Proj (1→M,(Array_Height+1)→N); //cropping out the padded space
elseif New_Rotation_Center_Row <(N/2)
    Padded_image= Pad_bottom(Original_image,Offset_Blank);
    Proj= rotate_crop(Padded_image, θ);
    Corrected_Proj= Proj(1→M,1→N); //cropping out the added space
else
    // if x_o happens to be in the centre no padding is needed
    Corrected_Proj= rotate_crop(Original_image, θ);
endif
```
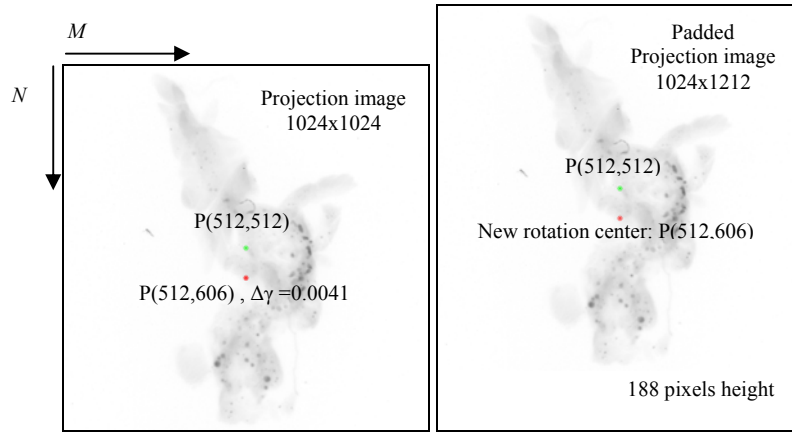
Fig. A2. The above padding algorithm implemented on a pancreatic specimen. (Left) the original projection image with the initial rotation central point and the point where the Δγ is closest to zero being superimposed. (Right) the same projection padded to centralize the rotation around the new found point.
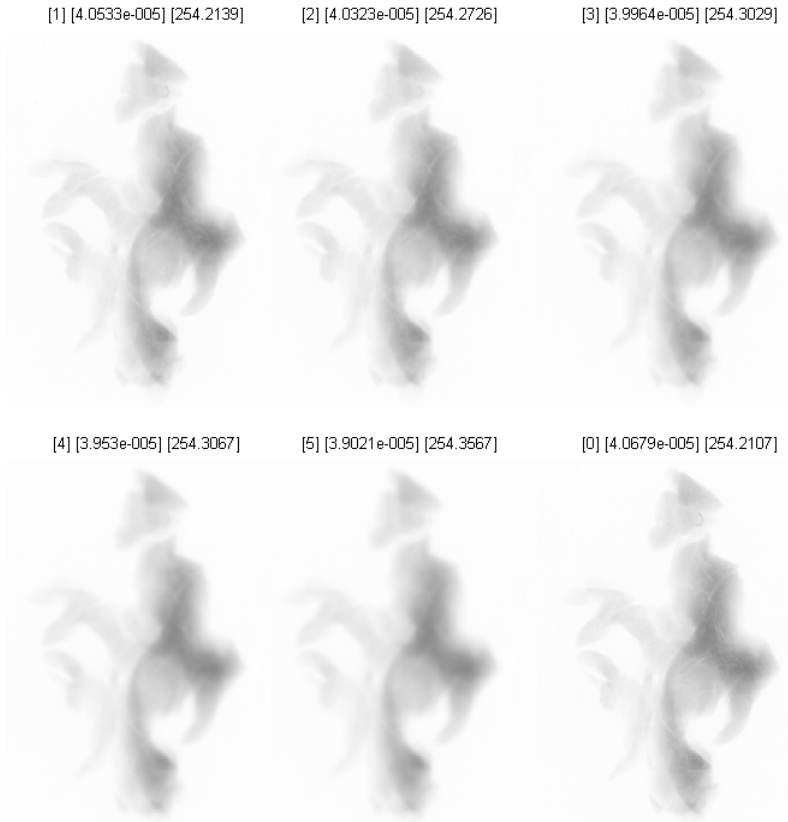

Fig. A3. Blurriness has a negligible effect on the performance of the proposed algorithms. The figure displays a projection view (GFP channel, size 512x512) of a pancreas with varying degrees of blurriness. The bracketed values correspond to the radius used in a circular averaging filter (pillbox) within a square block of size (2*radius+1), the 2D variance value and COM x-position (x_o), respectively. The bottom right image is the original (non-blurred) image. The blurring effect affects the precision of the COM-AR by less than half a pixel in the worst-case scenario, i.e., x_o=254.3567 (blurred image with radius 5) and x_o=254.2107 (non-blurred). When re-calculating the angle, index and correlation value using the most blurred image in the current example the derived parameters were: θ = -0.3572431, Index= 1254 and the correlation between the corrected pair=0.9816. For the non-blurred image the corresponding values were: θ = -0.3455803, Index= 1278 and the correlation between the corrected pair = 0.9877.

Supplementary Figures

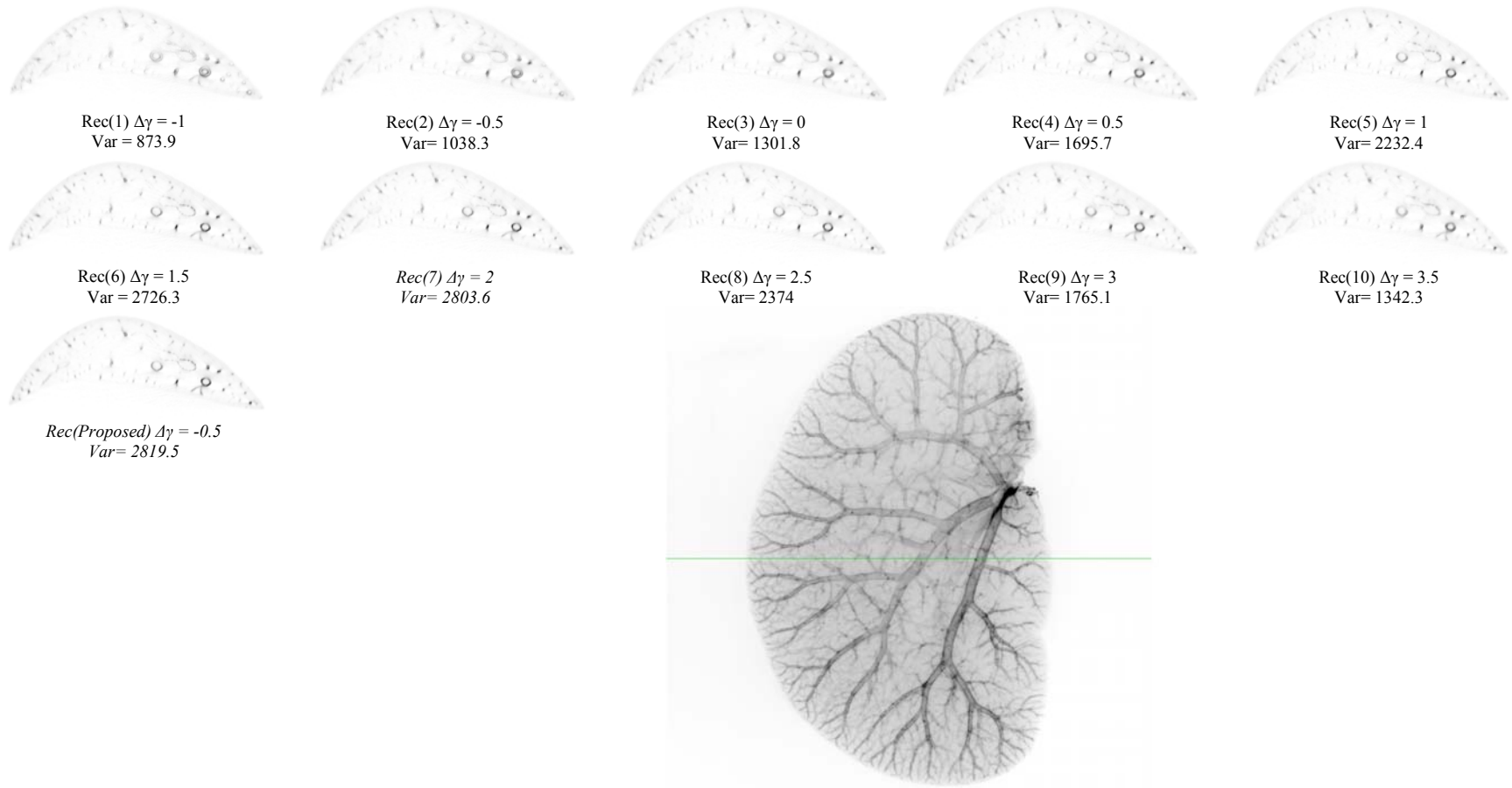Rec(1) Δγ = -1
Var = 873.9

Rec(2) Δγ = -0.5
Var= 1038.3

Rec(3) Δγ = 0
Var= 1301.8

Rec(4) Δγ = 0.5
Var= 1695.7

Rec(5) Δγ = 1
Var= 2232.4

Rec(6) Δγ = 1.5
Var = 2726.3

Rec(7) Δγ = 2
Var= 2803.6

Rec(8) Δγ = 2.5
Var= 2374

Rec(9) Δγ = 3
Var= 1765.1

Rec(10) Δγ = 3.5
Var= 1342.3

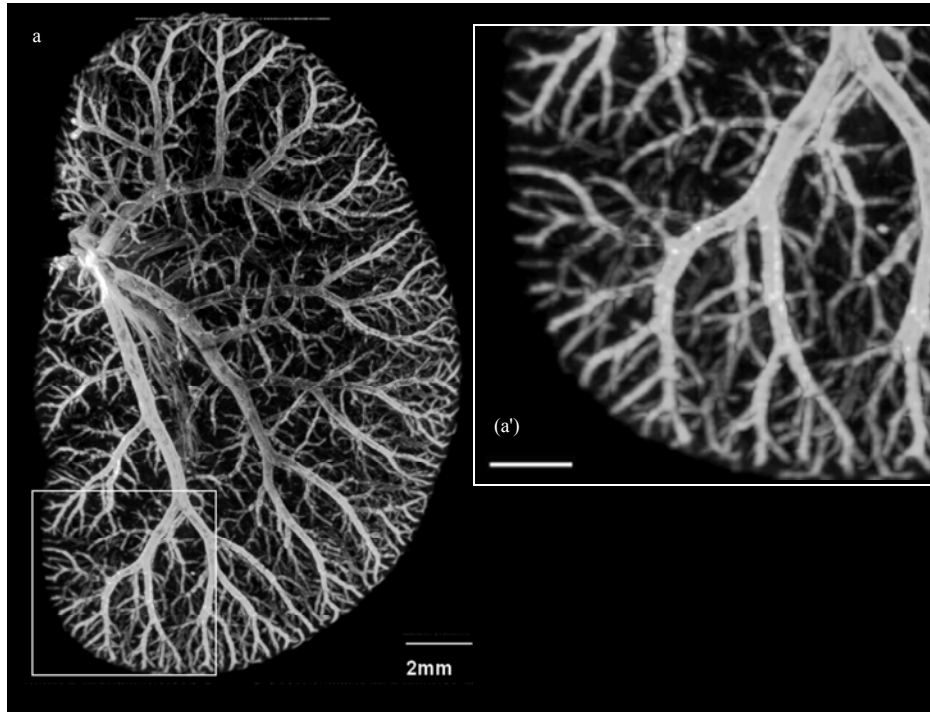*Rec(Proposed) Δγ = -0.5*
Var= 2819.5

Fig.S1. Visual comparison of variance-based corrections and the DFTA method on a liver specimen. The figure shows reconstructions of a single section from a 8 weeks female C57BL/6 mouse left lateral liver lobe, labelled with Cy3-conjugated anti-alpha smooth muscle actin antibodies which detects major blood vessels, using variance based correction (Rec(1-10)) and the DFTA method (Rec(Proposed)). Rec(1-10) correspond to reconstructions based on different Δγ values used as input to vote for the highest variance which eventually promoted Rec(7). Contrast this with the reconstruction using the proposed DFTA algorithm, Rec(Proposed). The proposed reconstruction was performed after Δγ correction using Angle = - 0.3852 and Index = 673. The reconstructed sections correspond to the green line in the projection image.
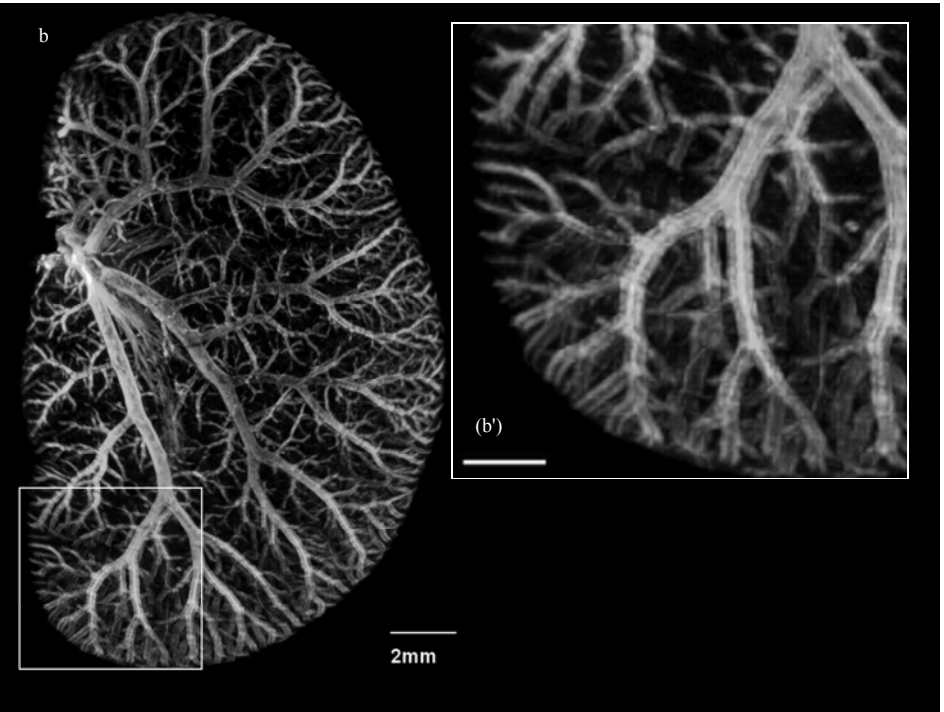
DFTA method

Variance-based method

Fig.S2. The proposed algorithms enhance image quality when applied to biological specimen. 3D volume rendering of the specimen seen in Fig.S1 using the proposed method (a, a' and Video III) and the variance -based method (b, b' and Video IV), respectively. (a') and (b'), close up of framed area in (a) and (b). In contrast to the variance-based method the proposed method produce images in which the reconstructed features (the outline of the blood vessels) are better preserved. Scale bar in a' and b' is 1mm.

Rec(1) Δγ = 11
Var = 68869.32

Rec(2) Δγ = 11.5
Var= 75861.11

Rec(3) Δγ = 12
Var= 82501.48

Rec(4) Δγ = 12.5
Var= 87037.42

Rec(5) Δγ = 13
Var= 86531.27

Rec(6) Δγ = 13.5
Var = 81852.83
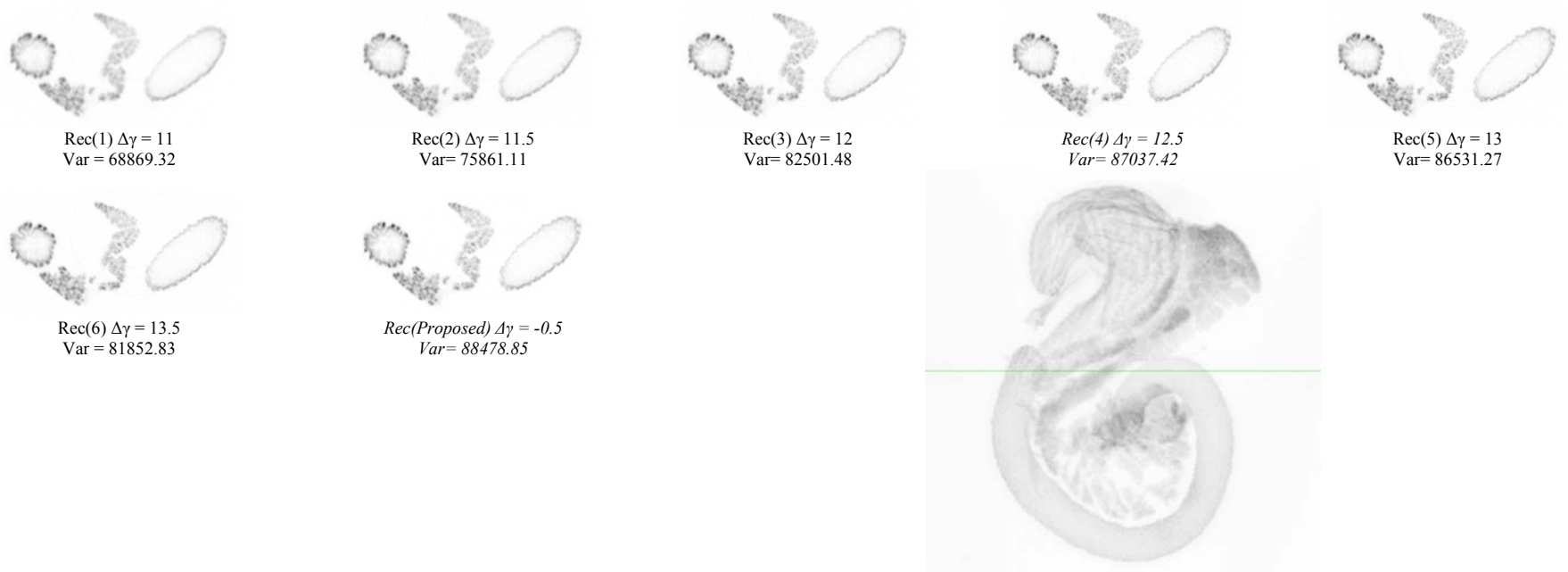
Rec(Proposed) Δγ = -0.5
Var= 88478.85

Fig.S3. Visual comparison of variance-based corrections and the DFTA method on a portion of the mouse gastrointestinal tract. The figure shows reconstructions of a C57BL/6 mouse embryonic day 17.5 gastro intestinal tract, labelled with E-cadherin antibodies which marks the gastrointestinal epithelium, using variance based correction (Rec(1-6)) and the DFTA method (Rec(Proposed)). Rec(1-6) correspond to reconstructions based on different Δγ values used as input to vote for the highest variance which eventually promoted Rec(4). Contrast this with the reconstruction using the proposed DFTA algorithm, Rec(Proposed). The proposed reconstruction was performed after Δγ correction using Angle =-0.240317 and Index = 3480. The reconstructed sections correspond to the green line in the projection image.
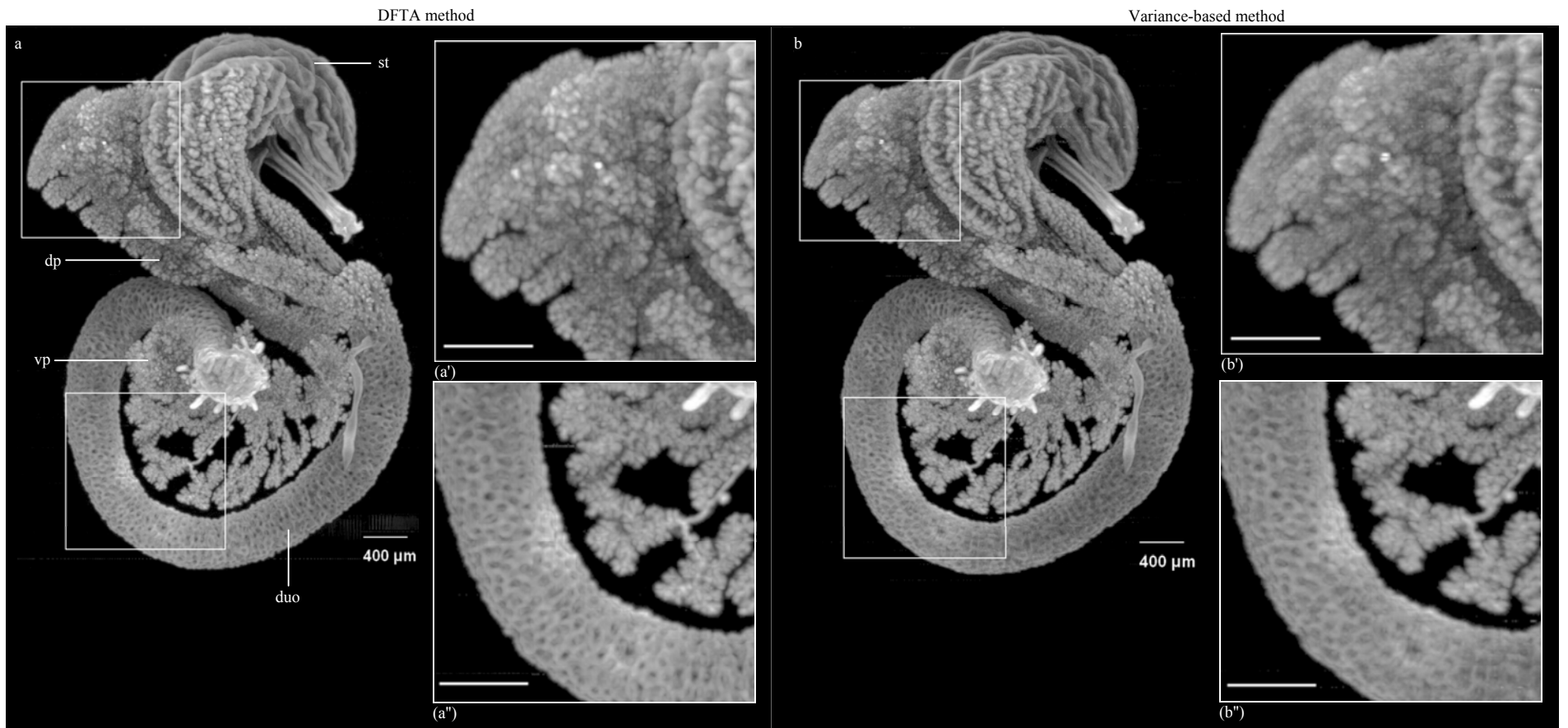
Fig.S4. The proposed algorithms enhance image quality when applied to biological specimen. 3D volume rendering of the specimen seen in Fig. S3 using the proposed method (a, a' and Video V) and the variance -based method (b, b' and Video VI), respectively. (a', a'') and (b', b''), close up of framed areas in (a) and (b). In contrast to the variance-based method the proposed method produce images in which the reconstructed features are better preserved, compare the outline of the branching pancreatic epthelium (a' versus b') and the crypts of the developing duodenum (a'' versus b''). Scale bar in a', a'', b' and b'' is 200 μm.
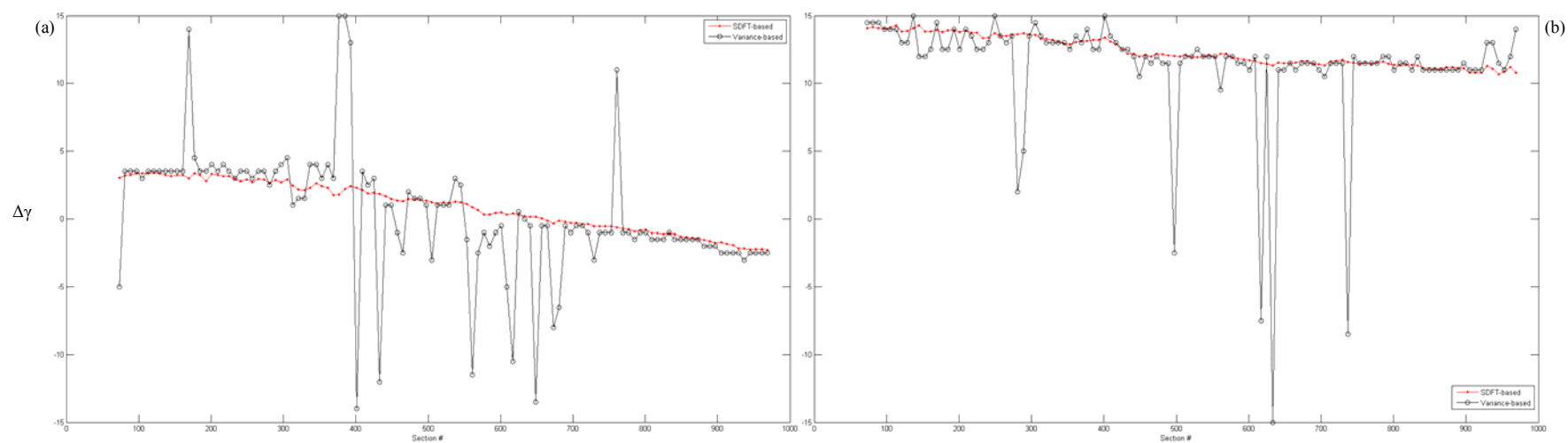
Fig. S5. Comparison of the calculated $\Delta\gamma$ values using the statistical variance versus the SDFT algorithm on the samples shown in Figs. S2 and S4. (a) A plot of $\Delta\gamma$ values using both methods derived from the liver sample shown in Fig. S2, and (b) a plot of $\Delta\gamma$ values using both methods derived from the mouse gastrointestinal tract sample shown in Fig. S4. The SDFT method yields a noticeable linearity across all sections. This linearity is crucial to find the proper parameters, i.e., the Angle and Index parameters, (see the discussion in relation to Fig. 10 in the manuscript).